

Communication

Simulations of Compression Ramp Shock Wave/Turbulent Boundary Layer Interaction Controlled via Steady Jets at High Reynolds Number

Tingkai Dai and Bo Zhang * 

School of Aeronautics and Astronautics, Shanghai Jiao Tong University, Shanghai 200240, China; jayddkt@sjtu.edu.cn

* Correspondence: bozhang@sjtu.edu.cn

Abstract: Shock wave/turbulent boundary layer interaction (SBLI) is one of the most common physical phenomena in transonic wing and supersonic aircraft. In this study, the compression ramp SBLI (CR-SBLI) was simulated at a 24° corner at Mach 2.84 using the open-source OpenFOAM improved delayed detached eddy simulation (IDDES) turbulence model and the “Rescaling and Recycling” method at high Reynolds number 1.57×10^6 . The results of the control effect of the jet vortex generator on CR-SBLI showed that the jet array can effectively reduce the length of the separation zone. The simulation results of different jet parameters are obtained. With the increasing jet angle, the reduction in the length of the separation zone first increased and then decreased. In this work, when the jet angle was 60° , the location of the separation point was $x/\delta = -1.48$, which was smaller than other jet angles. The different distances of the jet array also had a great influence. When the distance between the jet and the corner $d_{jet} = 70$ mm, the location of the separation point $x/\delta = -1.48$ was smaller than that when $d_{jet} = 65/60$ mm. A closer distance between the jet hole and the corner caused the vortex structures to squeeze each other, preventing the formation of a complete vortex structure. On the other hand, when the jet was farther away, the vortex structures could separate effectively before reaching the shock wave, resulting in a better inhibition of SBLI. The simulation primarily focused on exploring the effects of the jet angle and distance, and we obtained the jet parameters that provided the best control effect, effectively reducing the length of the CR-SBLI separation zone.

Keywords: CR-SBLI; rescaling and recycling; hybrid LES/RANS; jet control



Citation: Dai, T.; Zhang, B. Simulations of Compression Ramp Shock Wave/Turbulent Boundary Layer Interaction Controlled via Steady Jets at High Reynolds Number. *Aerospace* **2023**, *10*, 892. <https://doi.org/10.3390/aerospace10100892>

Academic Editors: Nick Zang and Tze How New

Received: 22 August 2023
Revised: 11 October 2023
Accepted: 17 October 2023
Published: 19 October 2023



Copyright: © 2023 by the authors. Licensee MDPI, Basel, Switzerland. This article is an open access article distributed under the terms and conditions of the Creative Commons Attribution (CC BY) license (<https://creativecommons.org/licenses/by/4.0/>).

1. Introduction

Shock wave boundary layer interactions (SBLIs) are flow phenomena that occur when shock waves interact with the turbulent boundary layer on a wall, causing changes in the flow field and wave system. SBLI is present in all practical transonic, supersonic, and hypersonic vehicles and engines, affecting their aerodynamic drag, heat transfer, and stability. By controlling these interactions, it is possible to improve performance and reduce risks associated with hypersonic flight. For example, on transonic wings, SBLI can lead to increased drag and instability, while in gas turbine engines, it can disrupt the flow of air into the compressor, reducing inlet efficiency. In supersonic flows, SBLI can cause the separation of internal flow and external flow, high wall heat flux, and pressure loss and deformation. In the rotary detonation engine (RDE), SBLI in the narrow channel can fundamentally affect its operation and lead to accidental ignition, resulting in the collapse of the rotational mode [1–5]. Therefore, it is imperative to use a boundary layer control system to mitigate the harm of SBLI by manipulating or modifying the flow field characteristics before or during the interaction to prevent or reduce separation caused by SBLI and flow unsteadiness, improving the aircraft and engine performance.

Initially, SBLI was studied via experimental methods such as schlieren visualization, oil flow, and sensors, which were later supplemented by Particle Image Velocimetry (PIV) and Non-intrusive Pressure and Temperature Sensitive Paints (NPLS), among others [6–9]. With the advent of computer technology, Computational Fluid Dynamics (CFD) became a popular tool in SBLI research, with simulations categorized into Reynolds-Averaged Navier–Stokes (RANS), Large Eddy Simulation (LES), and Direct Numerical Simulation (DNS). The RANS method, based on traditional turbulence models, can accurately predict time-averaged wall pressure but falls short in predicting the flow field’s topological structure and unsteady characteristics of the wave system and separation region. In contrast, LES and DNS can better reflect the flow field’s physical characteristics, but they are limited to medium and low Reynolds number conditions due to the Reynolds number barrier, and their computational cost is high. Therefore, there has been a developing trend towards employing hybrid LES/RANS turbulence models that offer high efficiency and accuracy for high Reynolds number cases [10].

The most widely used method for SBLI control was distributed suction and bleeding [11–13]. The suction method drained the boundary layer out of the flow by slotting or trepanning on the wall so that the freestream high-momentum fluid reoccupied the wall, thereby improving the fluid momentum and adverse pressure gradient resistance of the wall. Vortex-generating devices have also been studied. By generating flow vortices in front of the interacting region, momentum exchange was carried out between the main flow and the near-wall flow region, forming a fuller and more stable boundary layer [14–18]. Both passive and active vortex-generating devices have been studied in the past. The two methods were suitable for different application scenarios. The passive method used a fixed mechanical vortex generator to achieve this effect [19,20]. The cost of a mechanical vortex generator was lower. But, the problem with passive control was that the performance of aircraft was affected in off-design operating conditions. The steady air jet vortex generator [21–25] was an active method to produce the same effect. The steady air jet vortex generator can be switched on or off according to the application scenario [21]. Control can also be used in combination with transpiration cooling [22]. However, active control required additional energy, such as additional air paths for air jets. This increased the design difficulty and the cost of its manufacture and maintenance.

When the vortex generator has a height-to-boundary-layer thickness ratio (h/δ) greater than or equal to one, its presence can increase drag and reduce its control effectiveness [26,27]. To mitigate this effect, the size of the vortex generator can be reduced to be within the boundary layer. Micromechanical vortex generators or sub-boundary layer vortex generators with $h/\delta \leq 0.6$ incurred much smaller drag penalties [28–30], δ is the boundary layer thickness.

Various active control methods have been summarized in reviews by Lin [17], Lu et al. [18], Panaras and Lu [26], and Verma and Abdellah [31] have summarized various active control methods, including air jets, pulsed microjets [32,33], steady microjets [30,34,35], plasma jets [36], and synthetic jets [37]. The control effect of pulsed resonance-enhanced microjets has been demonstrated successfully [38], while other pulsed microjets based on piezoelectric [33] and microelectromechanical systems have also shown the same control effect [39]. The plasma jet has also shown good control ability in studies [36,40,41]. Furthermore, the jet can reduce the surface friction and the overall thickness of the boundary layer downstream of SBLI.

The simulation of CR-SBLI mainly focuses on the high-precision simulation of low Reynolds numbers, such as DNS and LES. However, at high Reynolds numbers, due to the Reynolds number barrier, hybrid LES/RANS is mainly used for simulation. Experimental methods are mainly used to verify the control effect of jet flow at compression corners. The experimental cost is high, and only one parameter can be studied in each experiment, there are few results from experiments. In this study, the control of the jet for CR-SBLI was simulated at a 24° corner at Mach 2.84 using the open source OpenFOAM IDDES

turbulence model and the “Rescaling and Recycling” method. By setting different jet angles and jet distances, the best control effect can be obtained.

2. Numerical Method

In this paper, the IDDES (Improved Delayed Detached Eddy Simulation) and “Rescaling and Recycling” methods are utilized as simulation methods. The IDDES method combines the advantages of RANS (Reynolds-Averaged Navier–Stokes) and LES (Large Eddy Simulation) by resolving the large-scale turbulent structures while modeling the small-scale turbulence. It provides a good balance between accuracy and computational cost. The “Rescaling and Recycling” method, on the other hand, is a technique used to simulate turbulent boundary layers. These two methods are briefly described in this paper to provide an understanding of the simulation techniques employed in the study.

The DES model can adopt RANS model in the boundary layer and LES model in the mainstream region, which can effectively reduce the amount of mesh used in the boundary layer and effectively avoid high Reynolds number barriers at high Reynolds number. The dissipation of turbulent kinetic energy via turbulent flow serves as a bridge between Reynolds-Averaged Navier–Stokes (RANS) and Large Eddy Simulation (LES). This ensures the return of the original model in the RANS region and allows for the Smagorinsky sub grid scale stress model to be obtained under the assumption of turbulent equilibrium in the LES region [42].

$$\bar{\rho}\varepsilon = \begin{cases} \text{LES region :} \\ \frac{\bar{\rho}k}{l_{LES}} = \frac{\bar{\rho}k}{C_{DES}\Delta}, C_{DES} = C_S \left[\frac{C_{\phi 1}}{(C_{\ell\varepsilon}C_{\phi 2})} \right]^{\frac{3}{4}} \\ \text{RANS region :} \\ \frac{\bar{\rho}k}{l_{RANS}} = \frac{\bar{\rho}k}{\left(\frac{1}{C_{\mu}^{\frac{1}{n}}}\right)^{\ell}}, \ell = C_{\ell}k^{\frac{m}{n} + \frac{3}{2}}\phi^{-\frac{1}{n}} \end{cases}$$

IDDES mixed length is defined as

$$l_{IDDES} = \bar{f}_d(1 + f_e)l_{RANS} + (1 - \bar{f}_d)l_{LES}$$

The core of the “Rescaling and Recycling” method is to estimate the velocity at the inlet plane based on the downstream fluid velocity. A velocity field is extracted from a plane near the outlet of the computational domain, and it is scaled using the theory proposed by Spalart and Leonard. Then, these data are reintroduced at the inlet as boundary conditions.

By defining the inner coordinates z_{inlt}^+ and outer coordinates η_{inlt} of a point on the entrance plane, as well as corresponding points z_{recy}^+ and η_{recy} on the recovery plane, the average and pulsating quantities of the flow velocity for the inner and outer layers can be recovered separately. This is achieved by combining Lund’s weight coefficients to obtain the instantaneous flow velocity on the entire entrance plane [43].

$$u_{inlt} = \left[U_{inlt}^{inner} + (u')_{inlt}^{inner} \right] [1 - W(\eta_{inlt})] + \left[U_{inlt}^{outer} + (u')_{inlt}^{outer} \right] W(\eta_{inlt})$$

$$W(\eta) = \begin{cases} \frac{1}{2} \left\{ 1 + \frac{\tanh\left[\frac{a(\eta-b)}{(1-2b)\eta+b}\right]}{\tanh(a)} \right\} & \text{for } \eta \leq 1 \\ 1 & \text{for } \eta = 1 \end{cases}$$

The “Rescaling and Recycling” method is extended to compressible flow based on Van Driest velocity transformation and temperature recovery adjustment.

3. Model and Grid in Numerical Simulation

The physical model is divided into two parts: the front “rescaling and recycling” plate domain and the compression corner of the main domain. The size of the front “rescaling and recycling” plate domain is $L_x \times L_y \times L_z = 4.342\delta \times 2.61\delta \times 2.17\delta$ (100 mm \times 50 mm \times 60 mm), and x , y , and z corresponded to the flow direction, normal direction and spanwise direction, respectively. The number of grids is $100 \times 150 \times 50$. The mesh of the “rescaling and recycling” plate domain is evenly distributed in the flow direction (x) and the spanwise direction (z), and the mesh is refined along the normal direction (y) close to the wall so that $y^+ \leq 1$. The compression corner of the main domain consists of an 80 mm plate and a 60 mm ramp with a spanwise length of 50 mm and a height of 50 mm. The number of grids is $188 \times 150 \times 50$. The mesh of the compression corner of the main domain is different for the x direction, the mesh around the corner is refined along the flow direction, and the mesh around the jet hole is refined along the x and y directions. This mesh refinement ensures that the jet and the flow structure around the corner are captured. The grid diagram is shown in Figure 1a.

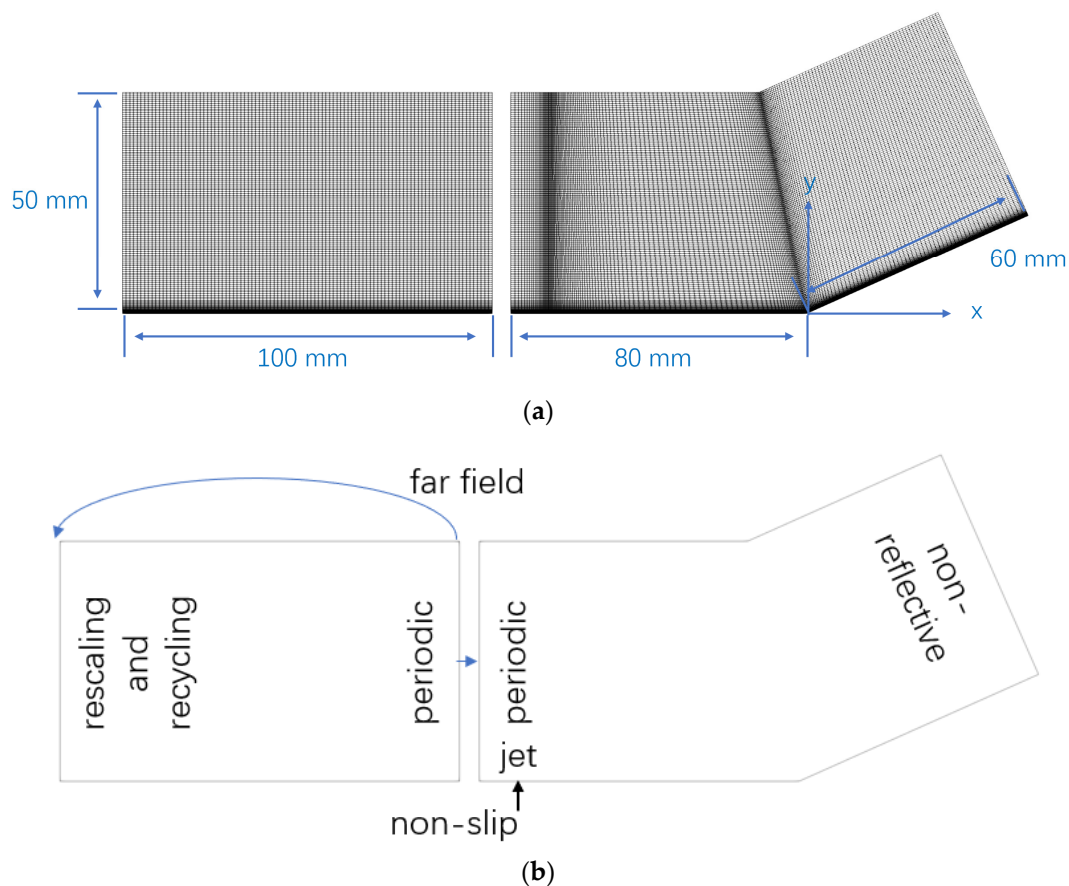


Figure 1. (a) Mesh and (b) boundary condition schematic layout of simulation.

In the plate domain, a “rescaling and recycling” inlet (including velocity and temperature “rescaling and recycling” inlets) is adopted at the entrance. The recycling and rescaling method is based on the turbulence boundary layer scaling principle. It involves defining a recycling plane downstream in the flow field, extracting the average and instantaneous parameters from this plane, adjusting them using the rescaling principle, and then recycling the adjusted parameters back onto the turbulence boundary layer generation plane. This process generates the parameters for the next time step on the recycling and rescaling computational domain, allowing for the rapid generation of the turbulence boundary layer. And the periodic boundary condition is adopted at the exit to recycle parameters to the inlet and pass the parameters down to the main domain. For the boundary conditions of the

main domain, the periodic boundary condition is used for the inlet boundary conditions to receive turbulence information obtained from the upstream. The outlet boundary adopts the non-reflective boundary pressure outlet condition to ensure that the outlet boundary type has no influence on the flow. The upper boundary conditions for both domains use the supersonic far-field boundary condition. The parameters are the same as the flow parameters, thus ensuring that the mainstream was consistent with the reference experimental conditions. The non-slip condition is adopted for the lower boundaries. The periodic boundary condition in the z -direction is also used for the lateral boundaries to ensure that the flow is not affected by the lateral boundaries. The jet inlet adopts a velocity boundary inlet because the direction of the jet needs to be changed. Here, the relevant jet velocity can be obtained via an equivalent calculation of jet pressure to realize jet flow. The two parts of the simulation domain are the same, the reason for the separation of planes is to input the parameters of the exit of the rescaling and recycling domain to the entrance, in the OpenFOAM the rescaling and recycling method must use periodic boundary conditions, the entrance of the main calculation domain is directly input from the recovery control calculation domain exit.

Referring to Settles' classic 24° CR-SBLI experiment [6] to set the physical parameters of the forward incoming flow at the entrance, the Mach number is $Ma = 2.85$ (velocity $U_{ref} = 585$ m/s), the far-field pressure is $P_{ref} = 23900$ Pa, and the far-field static temperature is $T_{ref} = 100$ K, the Reynolds number is 1.57×10^6 . The solver uses the supersonic unsteady solver sonicFoam based on pressure solution. The turbulence model is the IDDES $k - \omega$ SST hybrid LES/RANS turbulence model.

In this study, the diameter of the jet holes is 2 mm, the parameters here refer to the values of the relevant experiments [34]. Through the velocity equivalent of the experimental pressure, the velocity inlet is taken as the boundary condition of the jet inlet, and the jet velocity is 400 m/s. The number of jet holes is 5.

4. Results and Discussion

Firstly, the simulation of CR-SBLI without a jet is verified.

4.1. Plate Boundary Layer Simulation

The simulation of CR-SBLI via the hybrid LES/RANS method requires reasonable turbulence ahead. Figures 2 and 3 show the results of the front "rescaling and recycling" plate boundary layer at the outlet of the "rescaling and recycling" domain.

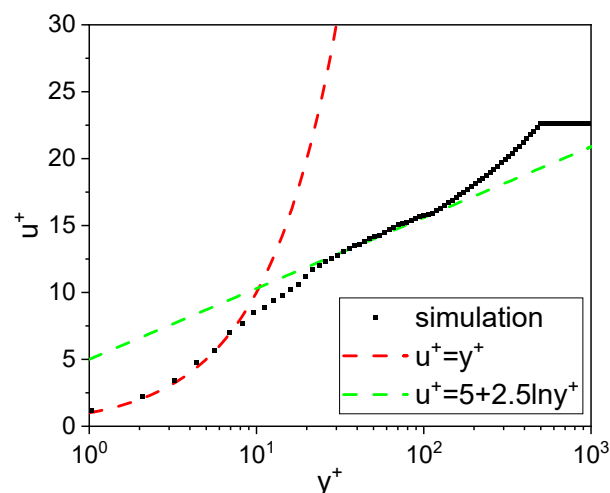


Figure 2. Velocity profile distribution in the turbulent boundary layer.

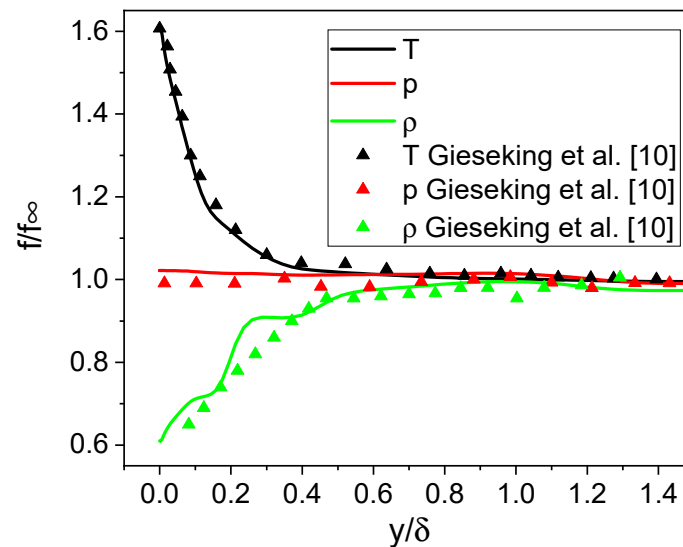


Figure 3. Distribution of the scalar field profile in the turbulent boundary layer.

Figure 2 shows the velocity profile distribution after the Van Driest transformation in the turbulent boundary layer. The black dots represent the simulation data, and the red and blue dashed lines represent the empirical formulas of the boundary layer velocity profile [6]. Morkovin's [44] hypothesis mentioned that when Mach number $Ma \leq 5$, the parameter distribution of the turbulent boundary layer of compressible flow can be associated with the parameters of the turbulent boundary layer of incompressible flow via Van Driest velocity transformation. The transformed velocity distribution satisfies well with the linear rate and logarithmic rate of the boundary layer and the wake region, as shown in Figure 2.

In addition to verifying the velocity profiles, this study also demonstrates, as shown in Figure 3, that the vertical distributions of other scalar fields, such as density (ρ) in green, pressure (p) in red, and temperature (T) in black, are consistent with the corresponding experimental data. The curves represent simulation data, and the dots represent the other simulation results [10]. The figure shows that the distribution of the three scalar fields was consistent with the experimental data, and the maximum error was less than 15%. The pressure distribution curve proves that there is almost no pressure gradient along the normal direction of the boundary layer. Therefore, the closer the wall, the lower the density and the higher the temperature of the fluid.

The "rescaling and recycling" method adopted in this study simulates the turbulent boundary layer structure well.

4.2. Grid Independence Analysis

Figure 4 presents a grid independence analysis of the model, where three types of grids (coarse, medium, and fine) with grid sizes of 1.23 million, 2.4 million, and 4 million cells, respectively, are used to simulate the same operating conditions. The coarse grid has a distribution of $164 \times 150 \times 50$, the medium grid has a distribution of $205 \times 187 \times 65$, and the fine grid has a distribution of $250 \times 200 \times 80$. The curves of the wall-averaged pressure for the 2.4 million and 4 million cell grids are almost identical at the separation point and pressure recovery values. This confirms the grid independence when using a grid size of 2.4 million cells, with a grid scale of 0.6 mm. For the simulation with the jet, except for the mesh refinement near the jet, the grid of this scale is used. Subsequent simulations are conducted using grids of a similar magnitude for grid partitioning. The time step is set to a variable step size to ensure that the Courant number is less than 0.3. After about 10,000 steps, the average velocity profile is consistent with the experimental data.

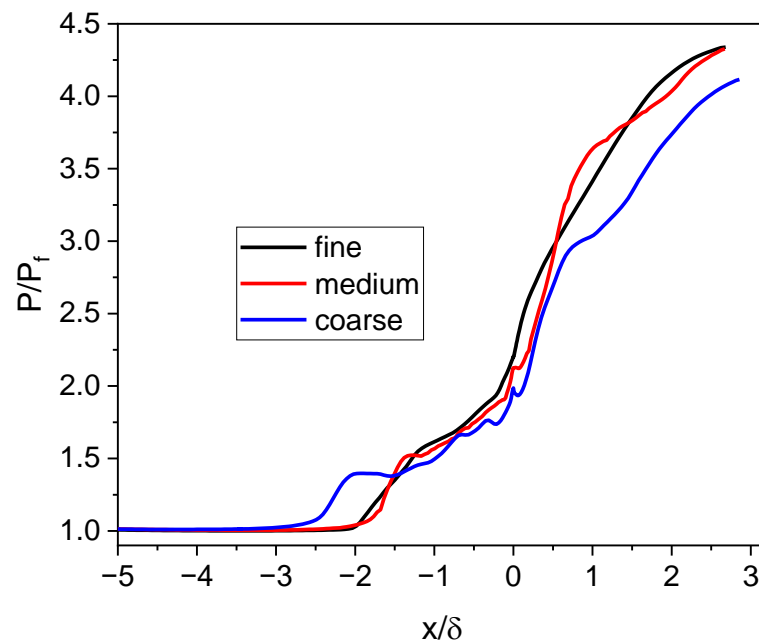


Figure 4. The compression ramp grid independence analysis.

4.3. Simulation of CR-SBLI

Figure 5 shows the three-dimensional turbulent structure of the compression corner identified using the Q criterion. Q criterion is a commonly used method for vortex identification. The vorticity structure of the turbulent boundary layer and SBLI can be observed by analyzing the Q criterion.

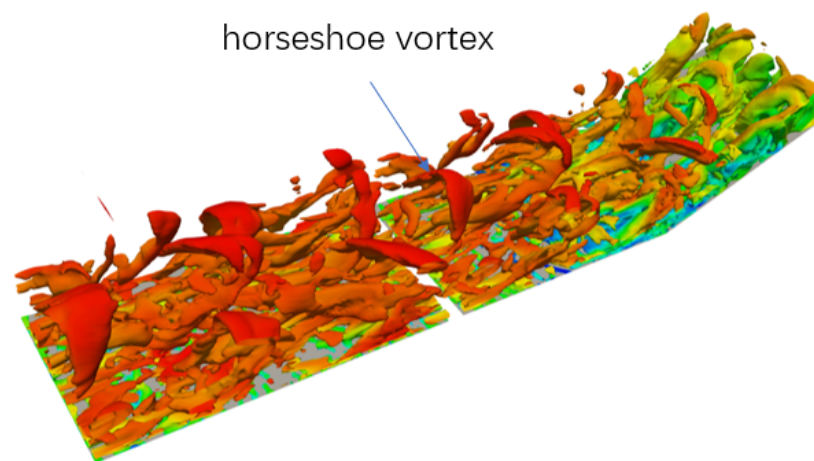


Figure 5. The vorticity field identified using the Q criterion for CR-SBLI.

Among them, the turbulent coherent structures of the turbulent boundary layer enabled the use of the Q criterion for identification, and the display is colored by velocity to show more details. The generated turbulence has an obvious three-dimensional structure. A typical horseshoe vortex structure, one of the typical structures of the turbulent boundary layer, is generated in the plate domain. The turbulent structure also continues to flow into the front of the corner in the main domain, and the identified turbulent coherent structure can be observed before the separating shock waves. However, when the three-dimensional vortex structure reaches the separation shock wave, it is obviously observed in the figure that the turbulent coherent structure identified by the Q criterion decreases. Here, the vortex structure is broken after the collision with the shock wave, and a smaller turbulent coherent structure is generated after the breakup. After entering the slope through the

corner, the turbulent coherent structure after the attached shock wave increases. However, the turbulence does not dissipate when leaving the interaction area, and there is still a turbulent coherent structure. According to the analysis of the Q criterion, the simulation results of this study obtained a clear vortex structure of CR-SBLI.

The wall pressure is extracted, and the boundary layer thickness at the outlet of “rescaling and recycling” δ and far-field pressure p_{ref} are taken as reference values to obtain the following curve of the wall pressure changing with the flow direction (x). Figure 6 shows the distribution of the average wall pressure along the flow direction in the main domain of the compression corner. At the same time, the simulation data are compared with the simulation data from Daniel et al. [10] and the experimental data from Settles [6]. The parameter x_{sep} is defined as the distance from the corner to the point of separation. The zero point of the x -coordinate is located at the corner, and the x -coordinate is dimensionless by taking the boundary layer thickness δ at the outlet of “the rescaling and recycling” domain as the reference length. It can be observed from the pressure distribution data that the position of separating shock waves in the experiment was $x_{sep} = -2.01$, while the position of separating shock waves in the simulation of the “rescaling and recycling” method in this study is $x_{sep} = -2.05$. The position of the DES simulation from Daniel et al. is $x_{sep} = -1.85$. Here, the position of the separating point of shock waves in this study is basically consistent with the experiment, with an error of 2%, and was closer to the experimental value than the simulation of the DES model.

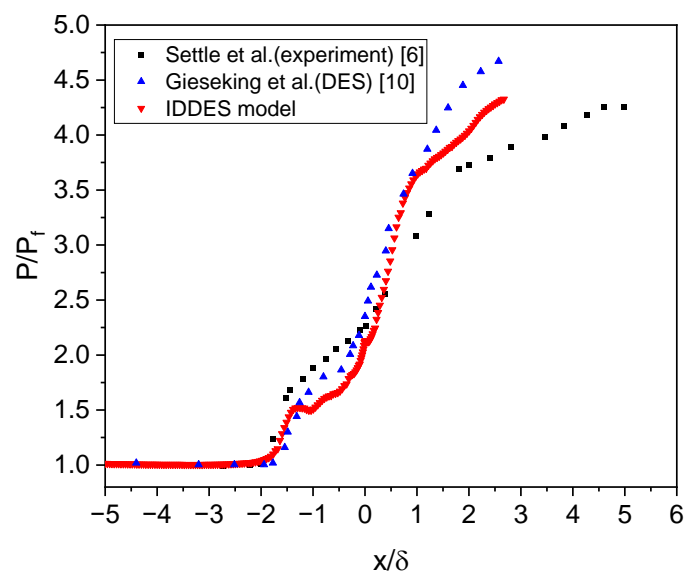


Figure 6. Pressure distribution along the centerlines of the wall for CR-SWBLLI.

4.4. Simulation of Jet Control

Figures 7 and 8 show the flow line slice diagram and the vorticity field identified using the Q criterion for CR-SBLI around the jet. The two figures are chosen for the condition that the jet hole is 60 mm away from the corner, where $d_{jet} = 60$ mm, and the jet angle is 60° as the flow field structure analysis. The distance between the jet holes is 7.2 mm. This value is based on the conclusions obtained in Verma’s experiments [45]. The jet directly interacts with the separation area along the main stream from the jet hole. In Figure 7, the effect of the jet on CR-SBLI is concentrated on the upper part of the separation zone, and the separation zone is reduced by squeezing the recirculation region. The black dotted line shows the case without any jet control. In Figure 8, the vortices generated by the jets from the jet array reach the separating shock waves without dissipating, thus interacting with the shock waves to control CR-SBLI.

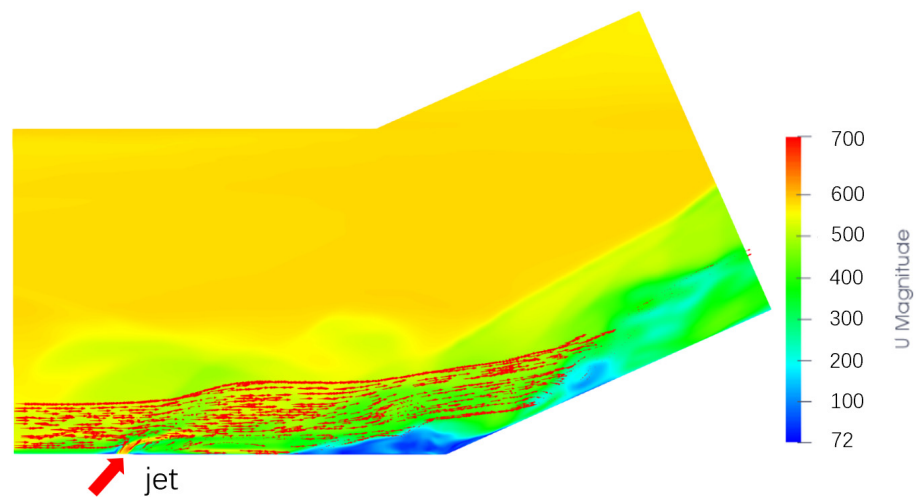


Figure 7. Velocity clouds and streamlines along the centerline section for CR-SBLI.

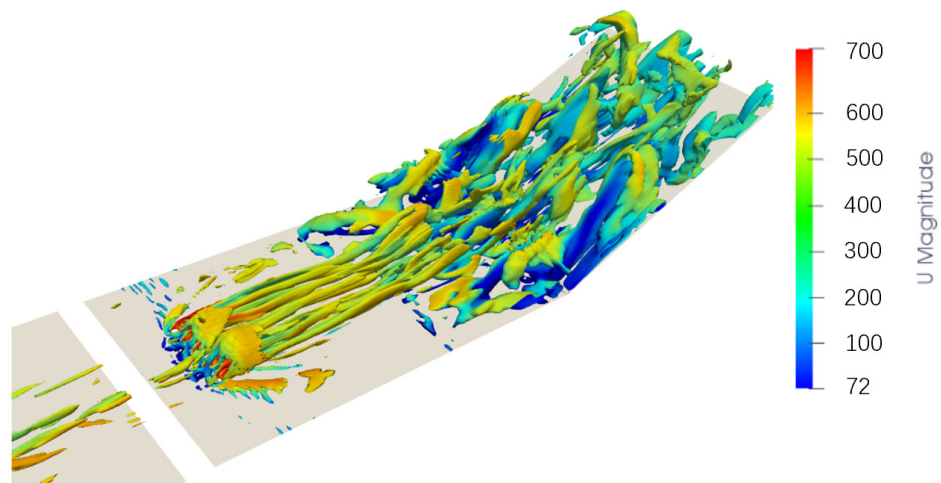


Figure 8. The vorticity field identified using the Q criterion for CR-SBLI around the jet.

4.5. The Effect of Jet Angle

Different jet angles have different influences on CR-SBLI. In this study, jet angles are set as 15° , 30° , 45° , 60° , and 75° to explore the influence of jet angle. Figures 9 and 10 show the pressure and velocity images near the jet under different jet angles, respectively. And Figure 11 shows the vorticity field identified using the Q criterion for different jet angles ($Q = 10^9$). From Figure 11, the vortex structure formed via the jet array becomes more obvious with increasing jet angle. In Figure 9, the larger the jet angle is, the larger the pressure change area near the jet holes, and the larger the jet action area.

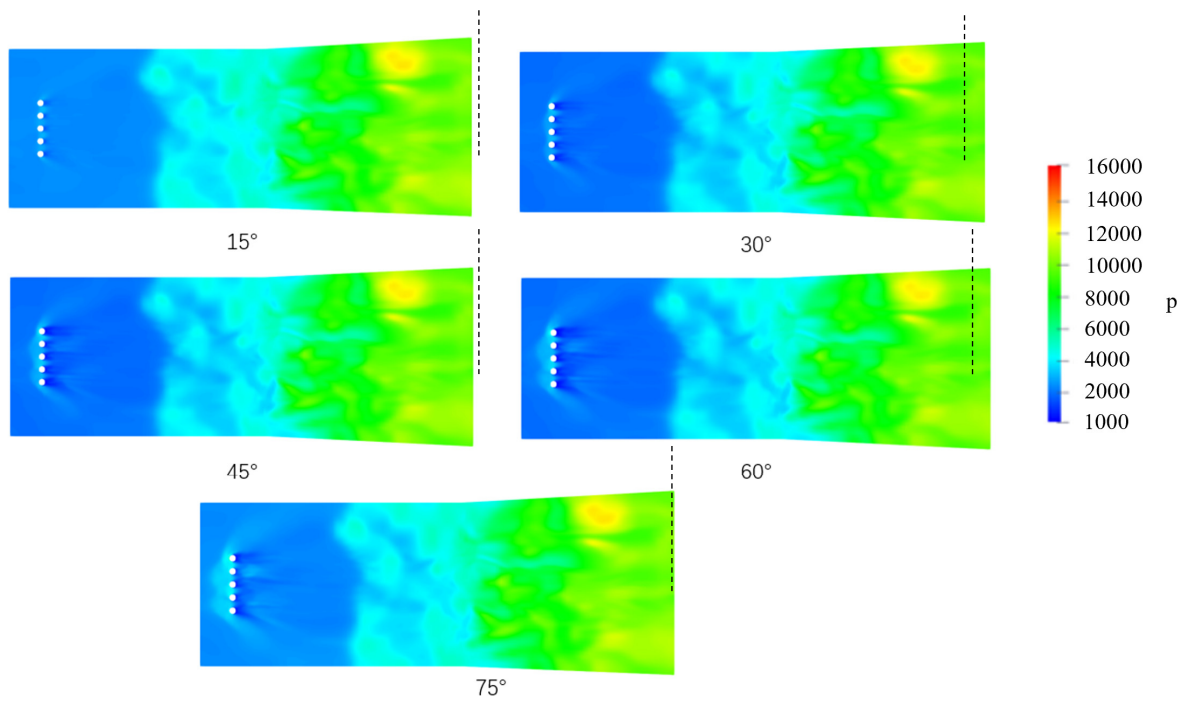


Figure 9. Comparison of pressure clouds along the walls for different jet angles.

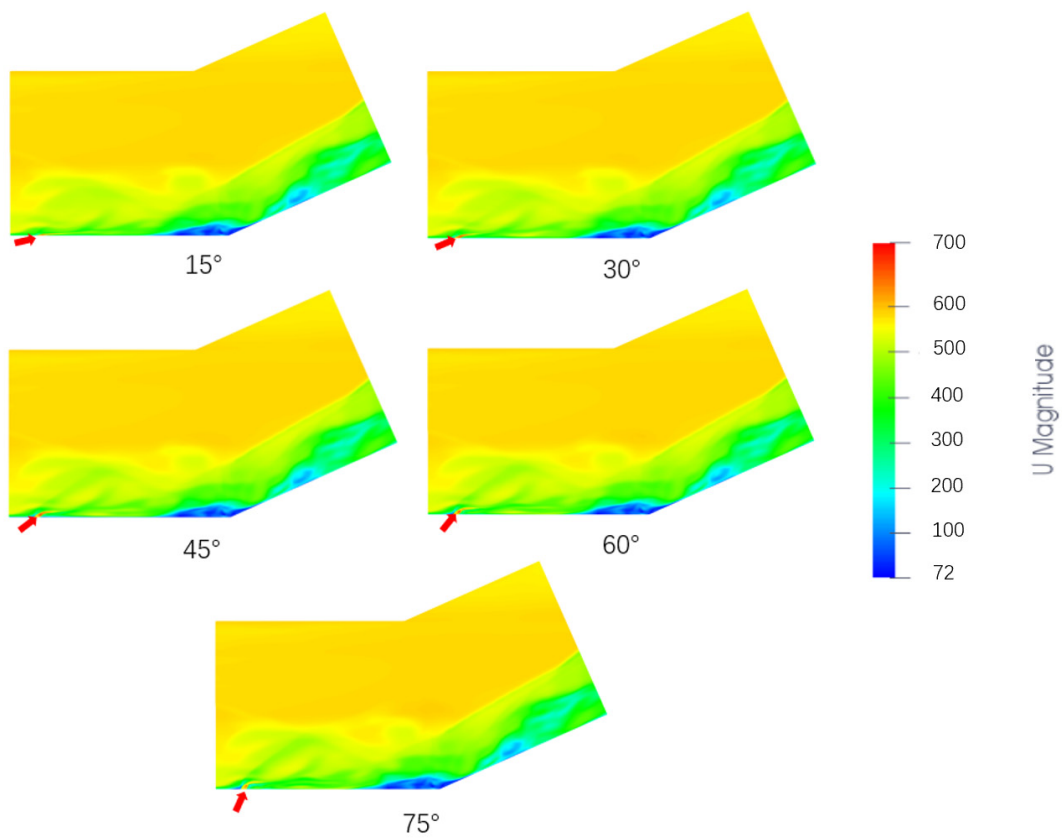


Figure 10. Comparison of velocity clouds along the walls for different jet angles.

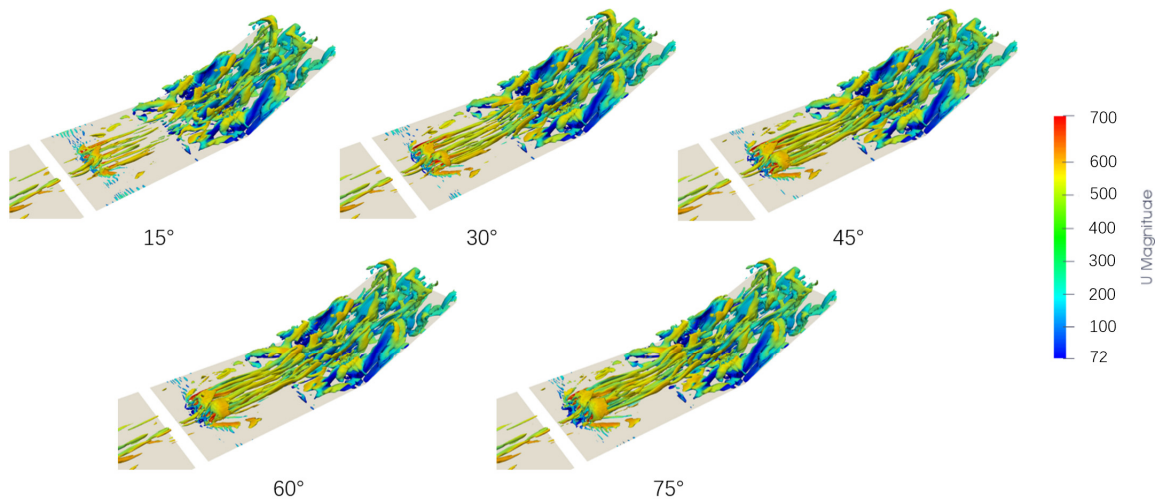


Figure 11. The vorticity field identified using the Q criterion for different jet angles.

The curve presents an up-and-down discontinuity at the position of the jet. The wall pressure distribution is shown in Figure 12, allowing us to better observe flow separation from CR-SBLI. The black curve shows the pressure distribution without jet flow. The position of separating shock waves without the jet in the simulation is $x_{sep} = -2.05$. Under the interaction of the jet, before 60° , the separation point gradually moves to the corner with increasing jet angle. After reaching 60° , the separation point position moves forward with the increasing angle. With increasing jet angle, the reduction in the length of the separation zone first increases and then decreases. In this work, when the jet angle is 60° , the jet has the best control effect on CR-SBLI separation.

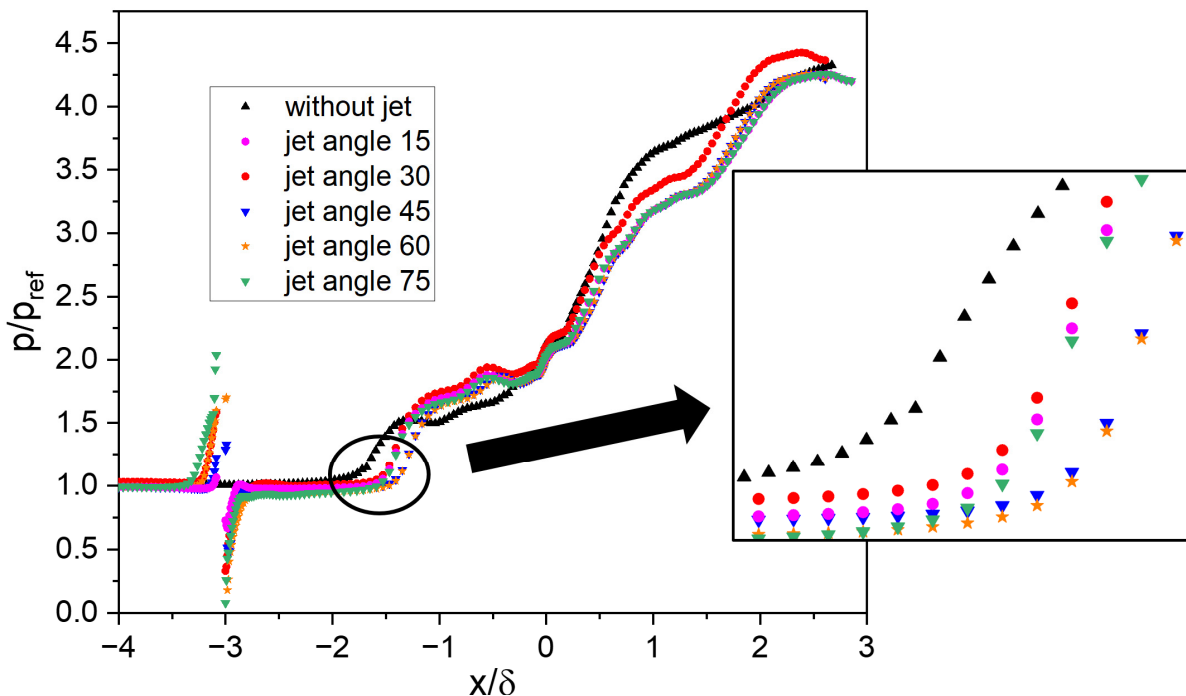


Figure 12. Comparison of pressure along the centerlines for different jet angles.

This phenomenon may be caused by the fact that when the jet angle is small, the jet flows close to the wall, and the vortex structure formed is not complete due to the existence of the wall. As the jet angle increases, the vortex structure is no longer affected by the wall surface, thus forming a complete vortex structure to flow to the CR-SBLI region, achieving

the best control effect. However, when the angle reaches a certain degree, the angle between the jet stream and the mainstream is too large, and the mainstream restrains the jet stream to a certain extent; thus, the effect becomes worse.

4.6. The Effect of Jet Distance

Figure 13 shows the instantaneous pressure images of the main domain of the compression corner under the action of jet arrays at three different distances. The parameter d_{jet} is defined as the distance from the jet holes to the corner. In Figure 13, under the interaction of jet flow, when $d_{jet} = 70$ mm, the separation area is smaller. When the jet is far enough away, the jet can further compress the separation zone so that the separation point of the separation zone is closer to the corner.

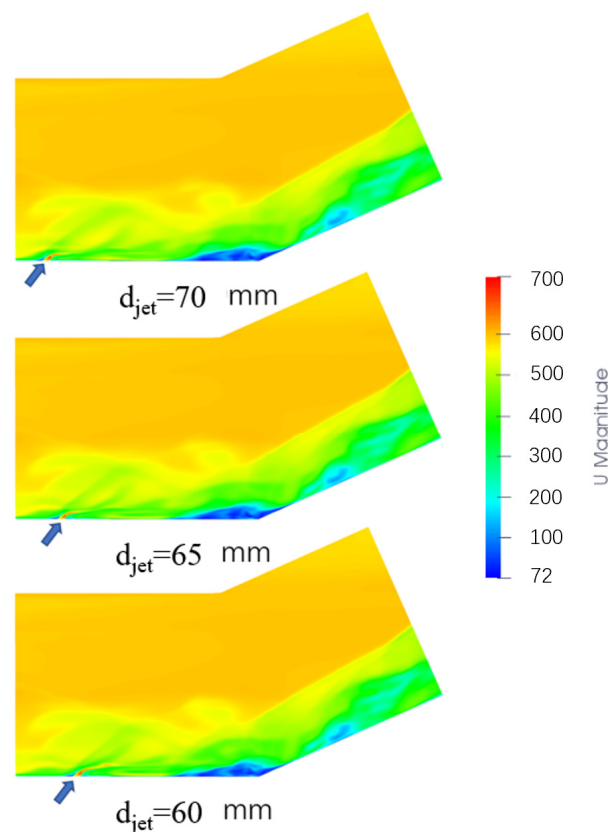


Figure 13. Comparison of velocity clouds along the walls for different jet distances.

Similar to Section 4.5 the wall pressure distribution is shown in Figure 14. Black represents the simulation condition without jet flow; red, blue, and green represent wall pressure curves with jet flow distance $d_{jet} = 70/65/60$ mm. Under the interaction of jet flow, the pressure separation point in the separation zone presented by three different jet flow distances is smaller than the separation point distance in the condition without jet flow. When $d_{jet} = 70$ mm, the location of the separation point $x_{sep}/\delta = 1.48$ is smaller than that when $d_{jet} = 65/60$ mm, and the inhibition effect on the separation zone is the best.

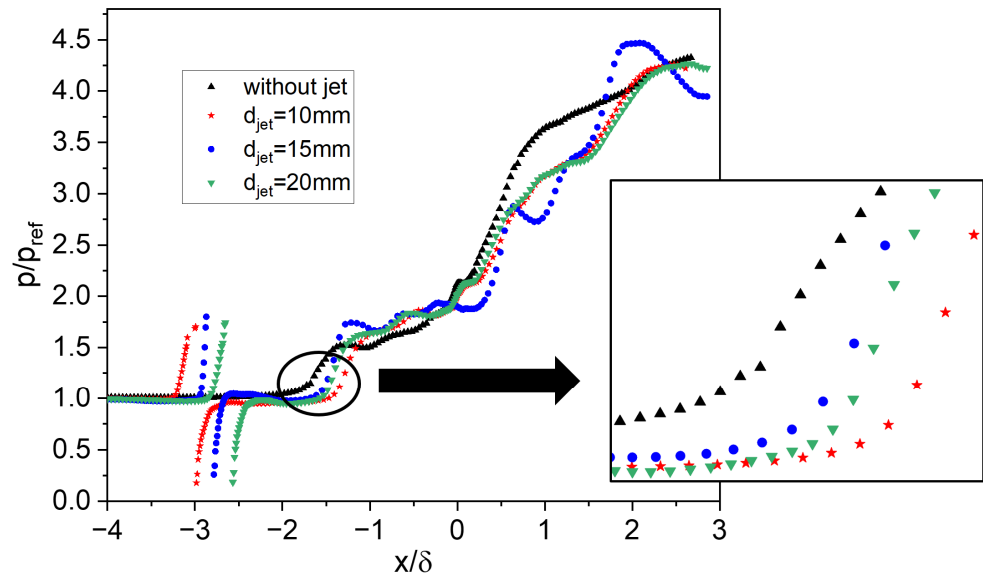


Figure 14. Comparison of pressure along the centerlines for different jet distances.

Taking 70 mm and 60 mm jet distances as examples, the effects of different jet distances are analyzed. According to the Q criterion diagram in Figure 15, when the jet distance is 70 mm, the vortex structure is dispersed when it reaches the shock wave. When the jet distance is 60 mm, the vortex structures push against each other in the shock wave. This phenomenon causes shock waves to squeeze and break each other, thus reducing the control effect of the vortex. When the jet distance is far away, it can be found that near the separation point, the vorticity identified using the Q criterion is far away from each other, and the interaction between vortices is not so strong. For jets with a relatively close distance, the vorticity identified using the Q criterion near the separation point is very close, which will cause the interaction between vortices. Therefore, the position of the jet should be maintained at a certain location upstream of the separation point. On the one hand, this avoids the dissipation of the vortex structure due to the jet position being too far away. On the other hand, it prevents the reduction of vortex structure intensity caused by the mutual compression at the initial stage of vortex formation, thus achieving a better control effect.

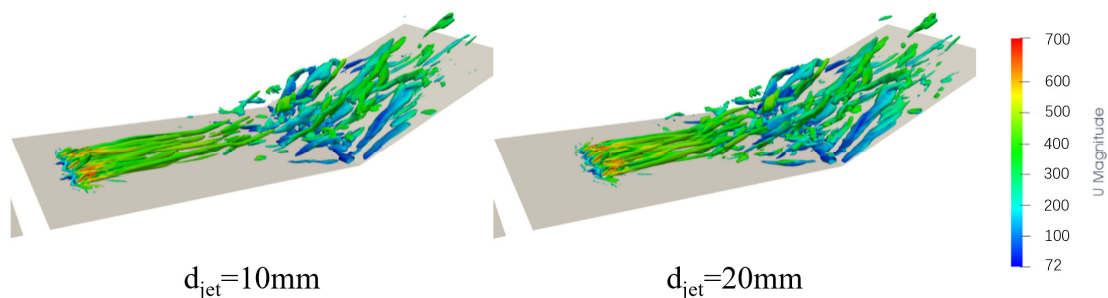


Figure 15. The vorticity field identified using the Q criterion for different jet distances.

5. Conclusions

In this work, the CR-SBLI phenomenon is simulated via the IDDES turbulence model and inlet turbulence generation technique of the compressible “rescaling and recycling” method at high Reynolds number 1.57×10^6 . The main conclusions are as follows:

Different jet angles of the jet array are simulated and compared, and five different jet angles of 15° , 30° , 45° , 60° and 75° are set. The jet flow at a 60° angle showed the best effect in reducing the length of the separation zone, as indicated by the wall pressure curve. As the jet angle increased, the reduction in the length of the separation zone initially increased and then decreased.

The simulations also compared different jet distances of the jet array, specifically 70 mm, 65 mm, and 60 mm from the entrance of the main domain. Among the three simulations, the jet array with a distance of 70 mm had the most significant effect in reducing the separation area. It is important to find a balance between the dissipation of vortices and the mutual compression of vortex structures by placing the jet at an optimal distance from the separation point.

Author Contributions: Conceptualization, T.D.; methodology, B.Z.; investigation, T.D.; writing—original draft, T.D.; writing—review and editing, B.Z.; supervision, B.Z.; funding acquisition, B.Z. All authors have read and agreed to the published version of the manuscript.

Funding: This research was funded by the National Natural Science Foundation of China (Grant Nos.: 12272234 and 91941301), the Innovation Program of Shanghai Municipal Education Commission (Grant No.: 2023KEJ105-75), and the Shanghai Science and Technology Planning Project (Grant No.: 22190711500).

Conflicts of Interest: The authors declare no conflict of interest.

References

1. Dolling, D.S.; Murphy, M.T. Unsteadiness of the Separation Shock Wave Structure in a Supersonic Compression Ramp Flowfield. *AIAA J.* **1983**, *21*, 1628–1634. [CrossRef]
2. Dussauge, J.-P.; Dupont, P.; Debiève, J.-F. Unsteadiness in shock wave boundary layer interactions with separation. *Aerosp. Sci. Technol.* **2006**, *10*, 85–91. [CrossRef]
3. Barter, J.W.; Dolling, D.S. Reduction of fluctuating pressure loads in shock/boundary-layer interactions using vortex generators. *AIAA J.* **1995**, *33*, 1842–1849. [CrossRef]
4. Yang, Z.; Cheng, J.; Zhang, B. Deflagration and detonation induced by shock wave focusing at different Mach numbers. *Chin. J. Aeronaut.* **2023**, in press. [CrossRef]
5. Zhang, B.; Li, Y.; Liu, H. Analysis of the ignition induced by shock wave focusing equipped with conical and hemispherical reflectors. *Combust. Flame* **2022**, *236*, 111763. [CrossRef]
6. Settles, G.S.; Vas, I.E.; Bogdonoff, S.M. Details of a Shock-Separated Turbulent Boundary Layer at a Compression Corner. *AIAA J.* **1976**, *14*, 1709–1715. [CrossRef]
7. Ganapathisubramani, B.; Clemens, N.T.; Dolling, D.S. Effects of upstream boundary layer on the unsteadiness of shock-induced separation. *J. Fluid Mech.* **2007**, *585*, 369–394. [CrossRef]
8. Ganapathisubramani, B.; Clemens, N.T.; Dolling, D.S. Low-frequency dynamics of shock-induced separation in a compression ramp interaction. *J. Fluid Mech.* **2009**, *636*, 397–425. [CrossRef]
9. He, L.; Lu, X.-g. Visualization of the shock wave/boundary layer interaction using polarization imaging. *J. Vis.* **2020**, *23*, 839–850. [CrossRef]
10. Gieseking, D.; Edwards, J. Simulations of a Mach 3 Compression-Ramp Interaction using LES/RANS Models. In Proceedings of the 49th AIAA Aerospace Sciences Meeting including the New Horizons Forum and Aerospace Exposition, Orlando, FL, USA, 4–7 January 2011; American Institute of Aeronautics and Astronautics: Reston, VA, USA, 2011. [CrossRef]
11. Seebaugh, W.R.; Childs, M.E. Conical shock-wave turbulent boundary-layer interaction including suction effects. *J. Aircr.* **1970**, *7*, 334–340. [CrossRef]
12. Tanner, L.H.; Gai, S.L. Effects of Suction on the Interaction between Shock Wave and Boundary Layer at a Compression Corner. 1967. Available online: <https://www.semanticscholar.org/CorpusID:14247426> (accessed on 20 August 2023).
13. Fukuda, M.K.; Hingst, W.R.; Reshotko, E. Bleed Effects on ShockA3oundary-layer Interactions in Supersonic Mixed Compression Inlets. *J. Aircr.* **1977**, *14*, 151–156. [CrossRef]
14. Giepmans, R.H.M.; Schrijer, F.F.J.; van Oudheusden, B.W. Flow control of an oblique shock wave reflection with micro-ramp vortex generators: Effects of location and size. *Phys. Fluids* **2014**, *26*, 066101. [CrossRef]
15. Rybalko, M.; Loth, E.; Chima, R.; Hirt, S.; DeBonis, J. Micro-Ramps for External-Compression Low-Boom Inlets. In Proceedings of the 39th AIAA Fluid Dynamics Conference, San Antonio, TX, USA, 22–25 June 2009. [CrossRef]
16. Babinsky, H.; Makinson, N.; Morgan, C. Micro-Vortex Generator Flow Control for Supersonic Engine Inlets. In Proceedings of the 45th AIAA Aerospace Sciences Meeting and Exhibit, Reno, NV, USA, 8–11 January 2007. [CrossRef]
17. Lin, J.C. Review of research on low-profile vortex generators to control boundary-layer separation. *Prog. Aerosp. Sci.* **2002**, *38*, 389–420. [CrossRef]
18. Lu, F.K.; Li, Q.; Liu, C. Microvortex generators in high-speed flow. *Prog. Aerosp. Sci.* **2012**, *53*, 30–45. [CrossRef]
19. Ashill, P.; Fulker, J.; Hackett, K. Research at DERA on sub boundary layer vortex generators (SBVGs). In Proceedings of the 39th Aerospace Sciences Meeting and Exhibit, Reno, NV, USA, 8–11 January 2001. [CrossRef]
20. McCormick, D.C. Shock/boundary-layer interaction control with vortex generators and passive cavity. *AIAA J.* **1993**, *31*, 91–96. [CrossRef]

21. Szwaba, R. Shock wave induced separation control by streamwise vortices. *J. Therm. Sci.* **2005**, *14*, 249–253. [[CrossRef](#)]
22. Souverein, L.J.; Debiève, J.F. Effect of air jet vortex generators on a shock wave boundary layer interaction. *Exp. Fluids* **2010**, *49*, 1053–1064. [[CrossRef](#)]
23. Evans, S.; Hodson, H. Separation-Control Mechanisms of Steady and Pulsed Vortex-Generator Jets. *J. Propuls. Power* **2012**, *28*, 1201–1213. [[CrossRef](#)]
24. Johnston, J.P.; Mosier, B.P.; Khan, Z.U. Vortex generating jets; effects of jet-hole inlet geometry. *Int. J. Heat Fluid Flow* **2002**, *23*, 744–749. [[CrossRef](#)]
25. Godard, G.; Stanislas, M. Control of a decelerating boundary layer. Part 3: Optimization of round jets vortex generators. *Aerosp. Sci. Technol.* **2006**, *10*, 455–464. [[CrossRef](#)]
26. Panaras, A.G.; Lu, F.K. Micro-vortex generators for shock wave/boundary layer interactions. *Prog. Aerosp. Sci.* **2015**, *74*, 16–47. [[CrossRef](#)]
27. Titchener, N.; Babinsky, H.; Loth, E. The Effects of Various Vortex Generator Configurations on a Normal Shock Wave/Boundary Layer Interaction. In Proceedings of the 51st AIAA Aerospace Sciences Meeting including the New Horizons Forum and Aerospace Exposition, Grapevine, TX, USA, 7–10 January 2013. [[CrossRef](#)]
28. Lee, S.; Loth, E. Impact of Ramped Vanes on Normal Shock Boundary Layer Interaction. *AIAA J.* **2012**, *50*, 2069–2079. [[CrossRef](#)]
29. Verma, S.B.; Manisankar, C. Assessment of Various Low-Profile Mechanical Vortex Generators in Controlling a Shock-Induced Separation. *AIAA J.* **2017**, *55*, 2228–2240. [[CrossRef](#)]
30. Verma, S.B.; Manisankar, C. Shockwave/Boundary-Layer Interaction Control on a Compression Ramp Using Steady Micro Jets. *AIAA J.* **2012**, *50*, 2753–2764. [[CrossRef](#)]
31. Verma, S.B.; Hadjadj, A. Supersonic flow control. *Shock Waves* **2015**, *25*, 443–449. [[CrossRef](#)]
32. Uzun, A.; Solomon, J.T.; Foster, C.H.; Oates, W.S.; Hussaini, M.Y.; Alvi, F.S. Flow Physics of a Pulsed Microjet Actuator for High-Speed Flow Control. *AIAA J.* **2013**, *51*, 2894–2918. [[CrossRef](#)]
33. Solomon, J.T.; Kumar, R.; Alvi, F.S. High-Bandwidth Pulsed Microactuators for High-Speed Flow Control. *AIAA J.* **2010**, *48*, 2386–2396. [[CrossRef](#)]
34. Ali, M.Y.; Alvi, F.S.; Kumar, R.; Manisankar, C.; Verma, S.B.; Venkatakrishnan, L. Studies on the Influence of Steady Microactuators on Shock-Wave/Boundary-Layer Interaction. *AIAA J.* **2013**, *51*, 2753–2762. [[CrossRef](#)]
35. Kumar, R.; Ali, M.Y.; Alvi, F.S.; Venkatakrishnan, L. Generation and Control of Oblique Shocks Using Microjets. *AIAA J.* **2011**, *49*, 2751–2759. [[CrossRef](#)]
36. Greene, B.R.; Clemens, N.T.; Magari, P.; Micka, D. Control of mean separation in shock boundary layer interaction using pulsed plasma jets. *Shock Waves* **2015**, *25*, 495–505. [[CrossRef](#)]
37. Vadillo, J.L.; Agarwal, R.K.; Hassan, A.A. Active Control of Shock/Boundary Layer Interaction in Transonic Flow Over Airfoils. In *Computational Fluid Dynamics 2004, Proceedings of the Third International Conference on Computational Fluid Dynamics, ICCFD3, Toronto, Canada, 12–16 July 2004*; Springer: Berlin/Heidelberg, Germany, 2006; pp. 361–366.
38. Alvi, F.S.; Lou, H.; Shih, C.; Kumar, R. Experimental study of physical mechanisms in the control of supersonic impinging jets using microjets. *J. Fluid Mech.* **2008**, *613*, 55–83. [[CrossRef](#)]
39. Joshua, H.; John, S.; Michael, H.; Farrukh, A.; William, O. Broadband pulsed flow using piezoelectric microjets. In *Active and Passive Smart Structures and Integrated Systems 2010*; SPIE: Bellingham, WA, USA, 2010; p. 76431V.
40. Narayanaswamy, V.; Raja, L.L.; Clemens, N.T. Characterization of a High-Frequency Pulsed-Plasma Jet Actuator for Supersonic Flow Control. *AIAA J.* **2010**, *48*, 297–305. [[CrossRef](#)]
41. Narayanaswamy, V.; Raja, L.L.; Clemens, N.T. Control of unsteadiness of a shock wave/turbulent boundary layer interaction by using a pulsed-plasma-jet actuator. *Phys. Fluids* **2012**, *24*, 076101. [[CrossRef](#)]
42. Wang, G.; Li, Q.; Liu, Y. IDDES method based on differential Reynolds-stress model and its application in bluff body turbulent flows. *Aerosp. Sci. Technol.* **2021**, *119*, 107207. [[CrossRef](#)]
43. Lund, T.; Wu, X.; Squires, K. Generation of Turbulent Inflow Data for Spatially-Developing Boundary Layer Simulations. *J. Comput. Phys.* **1998**, *140*, 233–258. [[CrossRef](#)]
44. Choi, J.-I.; Edwards, J.R.; Baurle, R.A. Compressible Boundary-Layer Predictions at High Reynolds Number Using Hybrid LES/RANS Methods. *AIAA J.* **2009**, *47*, 2179–2193. [[CrossRef](#)]
45. Verma, S.B.; Manisankar, C. Control of Compression-Ramp-Induced Interaction with Steady Microjets. *AIAA J.* **2019**, *57*, 2892–2904. [[CrossRef](#)]

Disclaimer/Publisher’s Note: The statements, opinions and data contained in all publications are solely those of the individual author(s) and contributor(s) and not of MDPI and/or the editor(s). MDPI and/or the editor(s) disclaim responsibility for any injury to people or property resulting from any ideas, methods, instructions or products referred to in the content.